



EUROPEAN ORGANIZATION FOR NUCLEAR RESEARCH

CERN-EP/79-31
11 April 1979

DETECTION OF FAR-ULTRAVIOLET PHOTONS
WITH THE MULTISTEP AVALANCHE CHAMBER.
APPLICATION TO ČERENKOV LIGHT IMAGING
AND TO SOME PROBLEMS IN HIGH-ENERGY PHYSICS

G. Charpak, S. Majewski^{*)}, G. Melchart and F. Sauli

CERN, Geneva, Switzerland

and T. Ypsilantis

DPhPE, CEN Saclay, Gif-sur-Yvette, France

ABSTRACT

We have designed and operated a multistep avalanche chamber capable of detecting single photons in the vacuum ultraviolet wavelength (130 to 160 nm). The device has been used to image photons generated from charged particles by Čerenkov effect in solid and gaseous radiators, and providing a ring pattern with a radius related to the particle's velocity; experimental values are given for the angle and velocity resolution obtained. Possible applications of the method for particle identification are discussed.

(Submitted to Nuclear Instruments and Methods)

*) On leave from the Institute of Experimental Physics, University of Warsaw, Poland.

1. INTRODUCTION: PREAMPLIFICATION AND TRANSFER OF IONIZATION ELECTRONS IN GASES

It has been shown recently^{1,2)} that with a proper choice of binary gas mixtures, A + B, a new variety of particle detectors can be built, based on the development of electron avalanches in uniform electric fields through a mechanism quite different from the one occurring in most proportional counters. The name multistep avalanche chamber (MSC) has been proposed for the new device.

In the carrier gas A, which according to our tests can be any of the noble gases, an electric field is applied with a strength such that free electrons experience non-ionizing inelastic collisions. These collisions lead, most probably via the production of dimers, i.e. molecular bound states of an excited atom and an atom in the ground state, to the emission of light quanta in a wide band centred around an energy characteristic of each gas. The process has been studied extensively³⁻⁶⁾ and is referred to as secondary light emission in the works on scintillating proportional counters⁷⁾.

When a small quantity of a gas B having an appropriate ionization potential is added to A, an efficient process of photoelectric reconversion takes place leading to an unusual photon-mediated avalanche growth¹⁾. In Fig. 1 we have represented the measured secondary light emission continua of several pure noble gases at atmospheric pressure, as well as the ionization potentials of vapours that can be used in conjunction. Since the absorption cross-section of all these vapours above the ionization threshold is around 50 Mb, the mean free path of photons is around 300 μm for a few per cent vapour addition at normal conditions: quantum efficiencies are typically around 50%. An electron avalanche developing under these conditions has several unusual properties, such as a large lateral spread that tends to obliterate any quantizing effect of discrete electrode structures (grids or wires), and the ability to "jump" through potential wells as observed in the development of the MSC. Consider indeed the three-electrode structure of Fig. 2, where a region P of high field E_p is followed by a region T of lower field E_T ; as shown in Fig. 2a, a fraction of the lines of force roughly equal to E_T/E_p escapes to the lower section. As represented schematically in

Fig. 2b, an electron accelerated in P induces the emission of a photon; a subsequent photoionization may then generate a new electron and the process continues, somehow resembling the usual avalanche multiplication. Photons released close to the central electrode may of course be reconverted in the region T, thus enhancing the purely electrostatic electron leak from P to T determined by the ratio of the fields and favoured by the lateral charge spread. The experimentally observed preamplification and transfer yields have been well reproduced using a Monte Carlo simulation; Fig. 2c shows, for example, the computed lateral avalanche spread obtained assuming a mean free path for both photon emission and reabsorption around 200 μm .

The possibility to transfer and drift a sizeable fraction of the preamplified electrons has led to the following development in the art of particle detection: the swarm of electrons can be transmitted through a grid to a new element where a second step of amplification occurs: a multiwire chamber, or another parallel-electrode avalanche chamber. Insertion in the drift space of a gating structure permits then to control the passage of the swarm and to admit to the second step only those electrons associated with preselected events. The delay introduced by the drift-time allows this type of decision with fast auxiliary counters for instance; this was the first motivation of the research. It permits the restriction of the total amplification to a selected class of events, thus considerably reducing the detrimental space-charge effects due to the accumulation of positive ions at high particle fluxes⁸⁾.

However the interest of the multistep approach appears to be broader:

- i) The fact that the second step may also be a parallel-grid counter opens the way to detectors without any thin amplifying wires. The difference with a single-step parallel-plate counter with the same total gain stems from the fact that the feedback mechanism mainly responsible for the discharge propagation in parallel-plate structures, namely the emission of ultraviolet (UV) light by the head of an avalanche and the subsequent release of photoelectrons at the cathode, is strongly suppressed by the transfer gap.

ii) The fact that the additive B is highly efficient for photoelectric conversion makes it an ideal detector for UV light of energy higher than its ionization threshold and lower than the cut-off of the window placed at the entrance of the structure. The intention of the present article is to illustrate some applications of the MSC in the last field.

2. THE MULTISTEP AVALANCHE CHAMBER AS A SINGLE PHOTON DETECTOR

It has already been demonstrated by the authors of Refs. 1 and 2 that in a multiple structure, where a preamplification and transfer element is followed by a conventional multiwire proportional chamber, large enough gains can be obtained to allow single photoelectron detection. Figure 3 (from the quoted works) shows the pulse-height spectrum recorded when illuminating the structure with an UV light source. The measured charge (about 1 pC peak) implied an effective chamber gain in excess of 10^6 and allowed detection and localization of single photons using the well-established bidimensional MWPC read-out techniques. Although not directly measured by the authors, the quantum efficiency of the device could be estimated from that known for the additive. In Fig. 4 we have represented the transmission properties of some commercially available window materials for far UV wavelengths^{*)}, as well as the quantum efficiencies of two additives used, benzene (C_6H_6)⁹⁾ and triethylamine [TEA, $(C_2H_5)_3N$]¹⁰⁾. For example, using benzene in argon with a thin LiF window allows average quantum efficiencies of around 25% in the photon energy range 9.2 to 10.6 eV (taking into account the window transmittance), as far as each converted photoelectron can be detected with full efficiency.

To study the detection and localization properties of the MSC for multiple photon events in this energy region, we have constructed the device represented in Fig. 5. A spark-plug is fired with an external high-voltage pulse, generating a burst of photons in an energy spectrum characteristic of the filling gas and whose quantity can be controlled by the discharge energy. The fraction of the photon spectrum that traverses the window can be absorbed in the chamber gas.

*) ORIEL Optik GmbH, Darmstadt, West Germany.

Although we could have used an electronic technique for charge localization^{2,11)}, it appeared that an optical recording on photographic plates was the most suited for a quick survey of simultaneous multiphoton events. The preamplification and transfer element of the MSC was therefore followed by a triggered spark chamber, as shown in the figure; the triggering time, in respect to the main plug sparking, was obviously determined by the electron's drift-time in the MSC. We may mention here that a device of this kind, named hybrid chamber, was operated long ago by Fisher and Shibata¹²⁾, although not for the same purposes. To obtain the best multitrack efficiencies the spark chamber had individually terminated 50 μm diameter wire electrodes, and a high-voltage square pulse about 100 nsec long was applied from a low impedance source at a time corresponding to the arrival of the preamplified electron swarm in the neighbourhood of the grounded electrode in the spark chamber. It was found that a transfer space at least 10 mm thick is necessary to avoid parasitic firing in the preamplifying gap because of capacitive pulse couplings. Using argon as gas filling in the spark-plug volume we could generate a burst of photons with a wavelength spectrum mostly below 150 nm, suited for this study¹³⁾. As filling for the MSC, we have tried several combinations of noble gases and photoionizing vapours, under the constraints imposed by the described preamplification and transfer mechanism; it appeared that the best multitrack efficiency in the spark chamber could be obtained using helium or helium-neon together with acetone or TEA (a well-known outcome of previous track chamber work¹⁴⁾). Although the secondary emission spectra of helium and neon are not known in our field conditions, their general behaviour under condensed discharge conditions suggests that photon emission takes place mostly around 80 nm¹³⁾, thus satisfying the described MSC operation constraint. Use of a low-density gas is also convenient in order to decrease the direct contribution of the ionization in the detector due to charged particles traversing the structure when one wants to detect, for example, the photons emitted by the particle by Čerenkov effect in a radiator (as we will see in the following sections).

The pictures in Fig. 6 show the images obtained in these conditions, with a mask placed in front of the chamber window to simulate a ring image, at an increasing number of photons in the burst. In Fig. 6c, the photoionization charge is so large as to result in a transition from the individual spark behaviour to a continuous glow regime. The ring mask diameter is 35 mm, with an opening of 0.1 mm; analysis of a succession of images like the ones shown confirmed the ability of the device to record multiphoton events with intrinsic accuracies better than a millimetre.

The charge signal induced on the preamplifying grid by single photoelectrons is far too small, at the present stage, to allow a self-triggered operation of the chamber. However, this can be realized using a strongly ionizing radiation source, as for example X-rays of several keV. In this case, the discriminated signal from the preamplification grid can be used to generate at the proper time the high-voltage pulse applied to the spark-chamber element and allows therefore the imaging of neutral radiation. Pioneering work on this matter was realized several years ago by Böhmer, using the hybrid chambers¹⁵⁾. The picture in Fig. 7a shows the image recorded with the chamber illustrated in Fig. 5 operated in the self-triggered mode and detecting 5.9 keV X-rays. In this case, the UV photon pulser was replaced by a non-collimated ⁵⁵Fe source, and the ring mask replaced by a 5 mm thick aluminium absorber with cross-shaped cutouts, with 2 mm wide openings, having arms of 40 and 20 mm length, respectively.

Increasing the voltage in the last section of the chamber, one can eventually get a d.c. operation of the system; Fig. 7b shows an example of the image obtained, with the same source and geometry, operating the device as a multistep spark counter. This mode of operation, different from that for the classic spark counter in that the total amplification process is separated in two steps, seems to have a considerably better stability of operation, an observation already made (although in a different context) by Aoyama and Watanabe¹⁶⁾. Obviously, the general background level in the d.c. mode is larger than for the pulsed operation, as one can see comparing Figs. 7a and b; this is due both to the larger values

of the applied voltages and to the cosmic radiation (the total exposure time to obtain the image in Fig. 7b was about 5 min).

3. IMAGING OF THE ČERENKOV LIGHT PRODUCED IN GASES

3.1 Introduction

A recent analysis¹⁷⁾ has shown that great advantages in Čerenkov detection techniques could be obtained by exploiting the quanta emitted in the far UV region where photoionization gaseous counters could be used, as they offer the possibility of detection and imaging of individual photons. Several groups have been working on this subject¹⁸⁻²⁰⁾, the key problem being to obtain large enough gains in a proportional chamber that maintains a good quantum efficiency; this is not a trivial issue, since large amplification factors can normally be obtained in proportional counters using organic quenchers that suppress the photon-propagated discharge or breakdown mechanism. As mentioned in the Introduction, the MSC approach defeats this otherwise fundamental limitation, allowing gains in excess of 10^6 to be obtained in gas mixtures with large quantum efficiencies in the far UV.

A simple optical arrangement, making use of a spherical mirror of radius r , permits the formation, on a spherical surface of radius $r/2$, of a ring image corresponding to all photons emitted in a transparent medium at an angle θ_c with the radiating particle trajectory. The radius, on the image surface, of the ring is given by

$$R = f\theta_c, \quad (1)$$

where f is the mirror focal length ($2f = r$). For $r \gg R$, a flat detection plane approximates well the spherical image surface and in this case the previous expression can be written as

$$R = f \tan \theta_c. \quad (1')$$

Since we will need them in the following analysis, let us here briefly summarize some relevant expressions concerning Čerenkov light emission^{21,17)}. Charged particles with velocity β (referred to the speed of light) emit Čerenkov radiation in a medium having the index of refraction n at an angle θ_c given by

$$\cos \theta_c = \frac{1}{n^3}, \quad (2)$$

above a threshold velocity given by $\beta = n^{-1}$. The refraction index is in general a function of photon frequency or energy, $n = n(E)$. The number of photons emitted in the energy range E_2-E_1 by a radiator of length L is given by:

$$N = \frac{2\pi\omega L}{hc} \int_{E_1}^{E_2} \left[1 - \frac{1}{[\beta n(E)]^2} \right] dE. \quad (3)$$

In computing the average number of detected photons, of course, one has to take into account all sources of energy-dependent efficiencies, like the absorption and reflection losses in the optical system, as well as the detection efficiencies. Assuming, in the energy interval E_2-E_1 , an average value n and ϵ for the refraction index and the over-all efficiencies, one can write

$$N = N_0 L \sin^2 \theta_c, \quad N_0 = 370 (E_2-E_1) \epsilon \quad (3')$$

(L in cm and E in eV). The velocity resolution obtainable from a ring radius measurement can be estimated by differentiation of expression (1') and substitution into Eq. (2):

$$\frac{\Delta\beta}{\beta} = \sin^2 \theta_c \frac{\Delta R}{R}. \quad (4)$$

Furthermore, if all sources of dispersion are Gaussian-like, the radius resolution when measuring N photons, assuming that the centre of the ring image is known, will be given by:

$$\left. \frac{\Delta R}{R} \right|_N = \frac{1}{\sqrt{N}} \left. \frac{\Delta R}{R} \right|_1, \quad (5)$$

the right-hand resolution corresponding to that for a single detected photon. A naive statistical argument based on the available degrees of freedom suggests that in case the centre point is unknown, and if the radius is computed from a fit to events with three or more photon points, the previous expression can be replaced by

$$\left. \frac{\Delta R}{R} \right|_N = \frac{1}{\sqrt{N-2}} \left. \frac{\Delta R}{R} \right|_1, \quad N \geq 3 \quad (5')$$

For small values of the Čerenkov angle, taking $\sin \Delta\theta_c \approx \Delta\theta_c$, and combining Eqs. (1), (3), and (5):

$$\Delta\theta_c \approx \frac{1}{\sqrt{N_0 L}} \left. \frac{\Delta R}{R} \right|_1 \quad (5'')$$

($\Delta\theta_c$ in radians). When approximation (5'') holds, one can see that the angular resolution is constant for a given geometry, i.e. independent of the Čerenkov angle. In practice, the major sources of dispersion in the radius measurement are the chromatic aberrations in the radiator and windows and the positioning errors in the photon imaging device. The first effect is particularly important in the far UV domain, since the index of refraction varies rapidly in this region.

2.2 Experimental observation of Čerenkov rings

We have constructed and tested a gas Čerenkov ring imaging detector, mounting the described MSC on a radiator tube, about 1 m long, operated in argon at a pressure slightly above the atmospheric one (Fig. 8). The focal length of the reflecting mirror, $f = 93$ cm, matched the distance between the mirror and the MSC. High-purity argon (3 ppm impurities, mostly water and oxygen) was used as radiator to minimize photon absorption; the mirror was coated with magnesium fluoride to provide a good reflectivity in the far UV (75% at 150 nm as given by the manufacturer). The MSC itself was operated with about 5% TEA in commercial grade helium; the system was installed in a 1.5 GeV/c non-separated charged particle beam at the CERN Proton Synchrotron, equipped with a gas threshold Čerenkov counter to identify the electrons (the only particles above threshold for this momentum). Several hundred pictures have been taken with a fast camera under these conditions. Because of the properties of the image-forming optics, of course, the direct ionization spark is located in the geometrical centre of the ring only for those particles whose trajectory coincides with the central axis of the system. Figure 9 shows an integrated image over ~ 30 events and gives an idea of the dispersion and the acceptance of the system; the Čerenkov photon ring appears clearly around the charged particle points, with a diameter of about 50 mm.

About 400 individual pictures have been hand-analysed by simple projection on a screen and with the following acceptance criteria:

- only centred events (i.e. with a spark in the fiducial volume corresponding to the beam collimation) were considered;
- the coordinates of all sparks, whatever their position, were measured in a reference system relative to this centre;
- a least squares fit to a circle (i.e. not using the centre constraint) provided the best estimate of the ring radius R for events having three or more photon points.

The measured photon number distribution is shown in Fig. 10 (points with error bars), together with the Poisson distribution for $\bar{n} = 1.7$ normalized to the same total number of events that represents the best fit to the data. Figure 11 instead shows the measured ring radius distribution, obtained as described for events containing three or more photons (about one hundred out of the total). The continuous curve is a Gaussian fit to the distribution with an average radius of 24.42 mm and a standard deviation of 2.05 mm (or about 8%).

Analysis of individual pictures reveals very little -- if any -- background that could be due to direct scintillation of argon in the sensitivity range of the MSC (an observation also made by the authors of Ref. 18).

2.3 Discussion of the data

From the measured value of the average ring radius, $\bar{R} = 24.42 \pm 0.22$ mm, and expression (1'), one can compute the average Čerenkov angle to be $\bar{\theta}_c = 1.50^\circ \pm 0.02^\circ$ and, from expression (2) for $\beta = 1$, the corresponding average index of refraction for argon in the detected wavelength domain, $(\bar{n} - 1) = (345 \pm 6) \times 10^{-6}$. This result is compared in Fig. 12 with the computed dependence of $(n - 1)$ for argon in the vacuum UV region²²), as given in the quoted reference at 0°C, 760 mm Hg and as computed in our conditions (20°C, 770 mm Hg) with an approximated density-dependent relationship. The approximate limits of sensitivity of our detector, using TEA and a calcium fluoride window, are also shown in the figure, the maximum quantum efficiency being around 150 nm (see Fig. 4).

In practice, several independent sources of dispersion limit the achievable radius resolution. In Table 1, we summarize the estimated value of the standard deviation of the single photon dispersion, assuming the central point to be known, for the following contributions:

- the chromatic aberrations in the gas, or the change in the refraction index with the detected photon energy in the sensitivity region; the known dependence of $n - 1$ from wavelength (Fig. 12) has to be folded in with the quantum efficiency of the detector, Fig. 4; this effect is obviously particularly large in the vacuum UV domain;
- the multiple scattering of the charged particle in the radiator producing a dispersion in the angle of the emitted photons, estimated as an average over the radiator length;
- the accuracy of localization of the detector itself and mainly of the spark chamber and associated optics.

As from Table 1, an over-all dispersion for single photons of around 1.2 mm standard deviation is expected from the three sources, a value to be compared with the observed 2.05 mm, obtained from a fit to mostly three photon events, under conditions where expression (5') would suggest a dispersion identical to the one for single photons with a known centre. We cannot explain the discrepancy so far, insisting however on the preliminary nature of our results.

The expected number of detected photons can be computed from expression (3), using approximate values for the efficiencies involved. Table 2 summarizes our estimates of the major losses, as due to the following effects:

- window transmittance at wavelengths around the detector sensitivity region;
- gas absorption, assuming 3 ppm of impurities with the oxygen cross-section around 150 nm (around 14 Mb);
- mirror reflectivity, given by the manufacturer to be around 75%;
- absorption in the first wire mesh of the detector, due both to its optical transparency (85%) and to the probability for the photoelectron to be captured by the mesh itself, if produced too close to the window; we have assumed a 30 μm dead layer for a 330 μm absorption length in the gas.

To these factors one has to add the integrated detector quantum efficiency; from Fig. 4 we estimate the average efficiency-energy product for TEA to be around 0.37 eV. From expression (3') and the data of Table 2, one gets therefore $N_0 \approx 44 \text{ cm}^{-1}$ and, for $L = 93 \text{ cm}$ and $\theta_c = 1.50^\circ$, $N \approx 2.8$ photons, larger than the

measured value ($\bar{N} = 1.7$, see Fig. 10). The more likely explanation for the discrepancy seems to us a larger residual oxygen contamination in the Čerenkov radiator, that could not for practical reasons be evacuated before the argon filling (since the CaF_2 window would not withstand the overpressure). A photon yield lower by a factor of two than the expected one was observed also by Chapman et al. under similar operating conditions¹⁸⁾. We cannot of course exclude an unknown source of inefficiency in the chamber itself.

4. USE OF FLUORIDE CRYSTALS AS RADIATORS

The UV transparent layer used as entrance window for the photon detector is itself a Čerenkov radiator for particles in the appropriate velocity range. In Fig. 13 we summarize the known values of the index of refraction for several fluoride crystals^{23,24)} (the corresponding UV cut-off was shown in Fig. 4). It is interesting to note that in the TEA sensitivity region, below 160 nm, all crystals (with the possible exception of magnesium fluoride) have an index that allows total reflection for the Čerenkov light emitted by particles perpendicular to their surface above a critical velocity. From simple optics and expression (2), total reflection is encountered at a critical velocity given by

$$\beta = \left[n \cos \arcsin \frac{1}{n} \right]^{-1}, \quad (6)$$

a condition that can only be satisfied for $n \geq \sqrt{2}$. For example, LiF, whose minimum index of refraction at the TEA ionization threshold is 1.47, outputs detectable UV Čerenkov radiation for normal tracks only in the velocity range $0.68 \leq \beta \leq 0.93$, a peculiarity that may offer interesting possibilities of application (see Section 5).

As in the case of a gaseous radiator, one has to make sure that direct scintillation in the radiator is not a substantial source of background. We have checked this point by mounting a commercially available UV sensitive photomultiplier with a magnesium fluoride window 1 mm thick^{*)} in a non-separated charged particle beam. The sensitivity range of the photocathode (CsTe) extends from

*) EMI Gencom Inc Type G26H315.

about 120 to 300 nm, a region where the index of refraction of MgF_2 is mostly below the total reflection limit. Figure 14 shows the measured pulse-height spectrum for 1.5 GeV protons and pions, traversing the window in the direction that allows the Čerenkov light to be detected on the photocathode, as well as the spectrum measured inverting the tube direction (for the same particle flux, lowest spectrum in the figure). Obviously, the extraction of direct secondary electrons from the photocathode or from the first dynodes may contribute to the last spectrum, giving evidence that direct scintillation, if any, is very small even in the extended sensitivity region of the tube as compared with TEA. Quite a different behaviour is expected in the visible range, where all fluorides are known to scintillate²⁵).

Since a large number of photons is emitted by such materials above threshold (they have a large index and therefore a large Čerenkov angle), thin radiators may be used thus allowing the simplification of the ring imaging optics. Figure 15 shows the arrangement we have tested; it consists of a 5 mm thick LiF window, used as radiator, 7.5 mm apart from an MSC with optical spark recording as described in Section 2. The chamber window is a 3 mm thick CaF_2 crystal. The ring image is here obtained by refraction of the light cone in the argon gap between the two windows, a considerable simplification in the optics which, however, has the disadvantage of providing an extra intrinsic dispersion due to the radiator width.

As for the gas radiator, several hundred pictures were taken in this geometry and a least squares fit to the measured photon points (if three or more) provided the best estimate of the image radius; some examples of individual events are given in Fig. 16. Again, the centre point could not be used (other than for consistency checks) since photons radiated in the MSC window are also detected and blur the charged track coordinate measurement. Figures 17 and 18 show, respectively, the measured distribution of the number of photons and of the reconstructed ring radius (for $N \geq 3$) for 1.3 and 1.5 GeV/c protons traversing the detector. The corresponding Čerenkov angles are 34.05° and 37.75° , well matched by the assumption of an average index of refraction for LiF of 1.50 (Fig. 19) consistent

with the known values (see Fig. 13). In Fig. 19 we have also represented the standard deviations in the angle estimate corresponding to the measured dispersion in R; for the restricted class of events (three or more photons) the equivalent velocity resolution is about 2% [see Eq. (4)]. Table 3 summarizes an estimate of the main effects contributing to the single photon dispersion, computed for 1.3 GeV/c protons; the over-all single photon dispersion corresponds to about 2.4 mm standard deviation. As the majority of the reconstructed events contains 4 or 5 photons at this momentum (see Fig. 17) the experimentally measured dispersion of 1.17 mm is consistent with expression (5').

The expected number of photons can be evaluated as for the previous case, taking into account reflection and absorption losses in the two windows; the contributions of the main sources of efficiency are given in Table 4, for 1.3 and 1.5 GeV/c momentum, respectively. For the estimate of the reflection losses on the crystal-gas interfaces we have used Fresnel's law for P polarized Čerenkov radiation; the average window absorption and quantum efficiency have been obtained from Fig. 4 as in the previous case. From expression (3'), therefore, we compute an average number of photons $N = 8.5$ and $N = 6.6$ for the two momenta. As for the case of the gas radiator, we are missing more than a factor of two in the photon yield, the discrepancy being particularly large for the higher momentum measurement, where however the large beam divergence and some misalignment may explain the losses, the Čerenkov angle being rather close to the one for total reflection in the radiator. Since in this case the gas purity is not of concern, we tend to believe in an unknown source of inefficiency in the MSC; alternatively, we may think of a badly degenerate transmission of the LiF crystal, a material that is known to be delicate to handle and that can substantially change its transmission properties at wavelengths below 200 nm²⁶). This point obviously requires further careful investigation.

5. FUTURE PROSPECTS AND APPLICATIONS

Detection of the Čerenkov rings by a photographic device, convenient for a rapid survey of the technique, may not be adapted to the present experimental requirements. On the other hand, the large number of simultaneous coordinates to

be measured prevents the use of conventional bidimensional multiwire chambers with either cathode-induced pulses or delay line read-outs because of poor multitrack and ambiguity resolution. Multicell structures with individual needle counters have been proposed¹⁷⁾ but they do not appear very simple to build. We are presently implementing a digital system having as a last step in the detector a multiwire chamber with current division read-out on the anodes where one expects, for moderate chamber sizes with 1 mm wire spacing, localization accuracies around 1 mm in both directions²⁷⁾. The ambiguity-free multihit capability remains, however, to be verified, since it could be worse than the simple wire spacing because of the large avalanche spread intrinsic in the MSC operation. It seems to us that coupling of an optical device of the kind described to a television-like scanning digitizer (like the plumbicon systems extensively used for spark chamber assemblies) may still offer distinctive advantages whenever large particle multiplicities and moderate data acquisition rates are expected.

Čerenkov light imaging using the MSC is of course restricted to the use of radiators that are transparent in the wavelength range between 120 and 160 nm. We have summarized in Table 5 the properties of some of them, giving the estimated value of the index of refraction^{22,23)} at 150 nm and the corresponding Čerenkov threshold [in terms of the velocity β or of $\gamma = (1 - \beta^2)^{-1/2}$]. For gases, the values are given at 0°C, 1 atm. Based on the previous results, one can estimate the expected resolution of an imaging counter; as an example in Fig. 20 we have represented the momentum dependence of the Čerenkov angle and of the ring radius for pions, kaons, and protons, obtained with a 50 cm long, 10 atm argon radiator. The width of the strips, one standard deviation each side of the average, has been estimated assuming a 10% relative radius accuracy determined by a single photon (an optimistic extrapolation of our previous results), combined with expression (5), and an average photon number given by Eq. (3), also indicated in the figure. The angular resolution is almost constant in all the range, corresponding to about 0.1°, as can also be inferred from the approximated expression (5').

For a Poisson-like distribution in the number of photons around the average, and requiring at least three photons detected to define a circle, we have estimated the constant inefficiency lines shown in the figure. Under these conditions,

a kaon-proton separation by more than three standard deviations can be foreseen from detection threshold (7.5 and 14 GeV/c for 10^{-3} inefficiency, for kaon and proton, respectively) up to about 28 GeV/c, an energy domain where kaon-proton identification is rather difficult using other techniques.

We may point out here that, contrary to photomultipliers, the MSC has a very little sensitivity to magnetic fields (only a small image shift may result at the strongest fields), and can in principle be operated at high pressures as far as the quenching vapour does not condense (its absolute amount should be maintained constant in the mixture, irrespective of the pressure, to keep a value of the absorption coefficient compatible with the MSC operation). One can therefore foresee the use of the gas detector even simply as replacement of a photomultiplier in threshold operated devices, in the presence of strong magnetic fields.

The use of fluoride radiators, as we have seen, allows the detection of Čerenkov photons emitted by particles above threshold velocities $\beta \approx 0.7$; this may be a handy device to identify short-lived, low-momentum particles in a detector only a few mm thick. Another attractive possibility is offered by the total reflection property, for particles normal to the radiator surface, above a critical velocity ($\beta \approx 0.93$ for LiF, see Section 4), which makes the detector insensitive to high-energy particles. One may think of using this peculiarity to search for or to identify rare, low-energy particles produced in a high flux of very relativistic tracks. We show in Fig. 21 a simple pulse-height measurement, obtained with an MSC similar to the one illustrated in Fig. 15 except that the terminal spark chamber was replaced by a conventional multiwire proportional chamber. The two pulse-height spectra show the measured yield under Čerenkov emission conditions in a 5 mm thick LiF radiator (larger peak, protons at 1.5 GeV/c), and under total reflection conditions (smaller peak, pions of the same momentum). The residual signal in the second case, which coincides with the spectrum obtained for both masses inverting the detector as compared to the beam direction, is given both by the direct ionization in the gas of the detector and by scintillation in the radiator. Obviously, the direct charge signal can be eliminated if one removes the MSC from the beam and uses a reflecting mirror.

REFERENCES

- 1) G. Charpak and F. Sauli, Phys. Lett. 78B, 523 (1978).
- 2) A. Breskin, G. Charpak, S. Majewski, G. Melchart, G. Petersen and F. Sauli, preprint CERN-EP/79-01, Jan. 1979, to be published in Nucl. Instrum. Methods.
- 3) J.R. Bennet and A.J.L. Collinson, J. Phys. B2, 571 (1969).
- 4) A. Gedanken, J. Jortner, B. Raz and A. Szöke, J. Chem. Phys. 57, 3456 (1972).
- 5) R.D. Andresen, E.A. Leiman and A. Peacock, Nucl. Instrum. Methods 140, 371 (1977).
- 6) M. Suzuki and S. Kubota, Mechanism of proportional scintillation in argon, krypton and xenon, submitted to Nucl. Instrum. Methods, Dec. 1978.
- 7) A. Policarpo, Space Science Instrum. 3, 77 (1977), and references therein.
- 8) G. Charpak, G. Melchart, G. Petersen, F. Sauli, E. Bourdinaud, P. Blumenfeld, C. Duchazeaubeneix, A. Garin, S. Majewski and R. Walczak, CERN 78-05 (1978).
- 9) J.C. Person and P.P. Nicole, ANL-7760 (1970).
- 10) G. Comby and T. Ypsilantis, private communication.
- 11) G. Charpak, G. Petersen, A.J.P. Policarpo and F. Sauli, Nucl. Instrum. Methods 148, 471 (1978).
- 12) J. Fisher and S. Shibata, Nucl. Instrum. Methods 401, 157 (1972).
- 13) Y. Tanaka, A.S. Jursa and F.J. LeBlanc, J. Opt. Soc. Amer. 48, 304 (1958).
- 14) G. Charpak and L. Massonnet, Rev. Sci. Instrum. 34, 664 (1963).
- 15) V. Böhmer, Fakultät für Physik der Universität Karlsruhe genehmigte Dissertation (July 1972).
- 16) T. Aoyama and T. Watanabe, Nucl. Instrum. Methods 150, 203 (1978).
- 17) J. Seguinot and T. Ypsilantis, Nucl. Instrum. Methods 142, 377 (1977).
- 18) J. Chapman, D. Meyer and R. Thun, Nucl. Instrum. Methods 158, 187 (1979).
- 19) R.S. Gilmore, J. Malos, D.J. Bardsley, F.A. Lovett, J.P. Melot, R.J. Tapper, D.I. Giddings, L. Lintern, J.A.G. Morris, P.H. Sharp and P.D. Wroath, An observation on the spatial distribution of vacuum UV photons generated by Čerenkov radiation, Univ. of Bristol preprint (July 1978).

- 20) S. Durkin, A. Honma and D.W.G.S. Leith, SLAC-PUB-2186 (1978).
- 21) J. Litt and R. Meunier, Ann. Rev. Nucl. Sci. 23, 1 (1973).
- 22) P.W. Langhoff and M. Karplus, J. Opt. Soc. Amer. 59, 863 (1969).
- 23) D.E. Gray (ed.), American Institute of Physics Handbook (McGraw-Hill, New York, 1963).
- 24) D.M. Roessler and W.C. Walker, J. Opt. Soc. Amer. 57, 835 (1967).
- 25) See, for example, K. Przibram, Irradiation colours and luminescence (Pergamon Press, London, 1956), p. 177 ff.
- 26) D.A. Patterson and W. Vaughan, J. Opt. Soc. Amer. 53, 851 (1963).
- 27) C.W. Fabjan, J. Lindsay, F. Piuz, F. Ranjard, E. Rosso, A. Rudge, S. Serednyakov, W.J. Willis, H.B. Jensen and J.O. Petersen, Nucl. Instrum. Methods 156, 267 (1978).

Table 1

Standard deviation of the single photon radius dispersion expected from the three major sources of diffusion in the argon radiator. The resulting over-all dispersion is about 1.2 nm.

Source	σ_R (mm)
Chromatic aberration	0.67
Multiple scattering	0.94
Detector	0.50

Table 2

Average estimated efficiencies for photon transmission due to the indicated effects in the argon radiator case. The over-all optical efficiency (not taking into account the detector quantum efficiency) is around 32%.

Source	ϵ
Window transmittance	0.65
Gas transmittance	0.86
Mirror reflectivity	0.75
Mesh transparency	0.77

Table 3

Standard deviation of the single photon radius dispersion expected for different reasons in the LiF radiator case for 1.3 GeV/c protons. The detector contribution includes also the spread introduced by the finite absorption length of photons in the gas (about 330 μm).

Source	σ_R (mm)
Radiator thickness (5 mm)	1.02
Chromatic aberration	1.99
Multiple scattering	0.26
Detector	0.77

Table 4

Average estimated efficiencies for photon transmission due to the indicated sources in the LiF radiator case. The over-all optical efficiency (not taking into account the detector quantum efficiency) is 40% and 26% for the two beam momenta, respectively.

Source	ϵ	
	1.3 GeV/c	1.5 GeV/c
Window transmittance	0.60	0.50
Interface reflections	0.98	0.88
Mesh transparency	0.70	0.60

Table 5

Refraction index around 150 nm and corresponding Čerenkov threshold for several materials transparent in the vacuum UV range. For solid fluorides and liquid neon the value given is an extrapolation of known values at longer wavelength (Ref. 23); for gases, the computed values of Ref. 22 are given, at 0°, 1 atm. For liquefied gases, the density-dependent expressions given in the same references have been used.

Radiator	n or $(n - 1) \times 10^{-4}$	β_T	γ_T
LiF	1.50	0.68	1.36
CaF ₂	1.57	0.63	1.28
Ne (Liquid)	1.10	0.92	2.49
He (Liquid)	1.03		
Ne	0.749		81.7
A	3.785		36.4
Kr	6.806		27.1
Xe	23.898		14.5

Figure captions

- Fig. 1 : Secondary photoemission spectra in several noble gases, measured at electric field values similar to the ones encountered in the multi-step chamber (from Ref. 6). The ionization potentials of acetone, benzene and triethylamine (TEA) are also shown.
- Fig. 2 : Photon-mediated preamplification and transfer mechanism in gases, in a three-electrode structure. Electrons produced in the upper region experience inelastic collisions with the molecules of the main constituent, A, of the gas mixture, which lead to the emission of photons; some of them are reconverted to electrons by photoionization of component B. There results a large, concentration-controlled lateral spread of the avalanche, which permits obliteration of the quantizing effects of the central electrode wires. Transfer of charges from the upper to the lower region is controlled by the ratio of the fields.
- Fig. 3 : Pulse-height spectrum for single photoelectrons generated by a UV lamp in a multistep avalanche chamber (MSC) (from Ref. 1).
- Fig. 4 : Compilation of the quantum efficiency of benzene⁹⁾ and TEA¹⁰⁾, and of the window transparency for 5 mm thick crystals^{*}) as a function of photon wavelength.
- Fig. 5 : Testing the imaging capability in the vacuum UV for multiphoton events with the MSC. Bursts of photons are generated in argon by the triggered spark plug, and a mask in front of the detector allows the simulation of a ring image. The MSC in this case consists of a preamplification and transfer element followed by a triggered spark chamber. The gas filling that provides the best multiphoton efficiency appeared to be helium or helium-neon (Henogal) in conjunction with 2 to 5% of acetone, benzene or TEA.

^{*}) OREL Optik GmbH, Darmstadt, West Germany.

- Fig. 6 : Ring images obtained by a photographic recording of single events, at an increasingly large number of photons generated by the spark plug of Fig. 5. The ring diameter and width are 35 and 0.5 mm, respectively (polaroid film, 3000 ASA, opening 5.6).
- Fig. 7 : Imaging soft X-rays (5.9 keV) with the multistep spark chamber. In (a), the image is obtained operating the device in the self-triggered mode, the HV pulse to the spark chamber being initiated by the signal detected on the preamplification element. In (b), instead, the same image is obtained operating the chamber as a d.c. spark counter.
- Fig. 8 : Čerenkov ring imaging with a gas radiator (argon at normal conditions). The optical system (mirror and window) is optimized for good response in the far UV region of sensitivity of the detector, around 150 nm. The MSC detector itself is the same as the one illustrated in Fig. 5, and photographic recording of individual events is obtained by a fast camera as represented.
- Fig. 9 : Integrated image over ~ 30 events obtained with the apparatus shown in the previous figure. The Čerenkov ring pattern appears clearly, with a radius of about 25 mm; the central spot corresponds to the overlap of the sparks developing on the direct ionization of the beam particles (1.5 GeV/c electrons). The small amount of off-ring counts proves that direct scintillation in the radiator is almost negligible.
- Fig. 10 : Measured distribution of the number of photons (points with error bars) as recorded with the detector of Fig. 8 on 1.5 GeV/c electrons. The histogram represents a Poisson distribution for the same number of events, computed for an average of 1.7 photons.
- Fig. 11 : Measured distribution of the average ring radius (points with error bars), obtained from events having three or more photon points. The full curve represents a Gaussian fit with average value and standard deviation as indicated.

- Fig. 12 : Comparison between the computed index of refraction for argon²²⁾ in the far UV, at 0°C, 760 mm Hg (full curve) and in our conditions at 20°C, 770 mm Hg (broken curve), and the average value provided by our measured Čerenkov ring radius; the detector sensitivity range is shown, peaked around 150 nm.
- Fig. 13 : Known dependence of the refraction index in the far UV for several fluoride crystals^{23,24)}.
- Fig. 14 : Pulse-height spectrum measured on a 1 mm thick MgF₂ window with a UV-sensitive phototube, for 1.5 GeV/c protons and pions traversing the system so that the Čerenkov light emitted by the crystal could be directly detected on the photocathode. The smaller peak corresponds to the same total exposure to the beam, having turned the system by 180°.
- Fig. 15 : The MSC used for imaging the photons emitted by Čerenkov effect in a 5 mm thick LiF radiator. The chamber window is a 3 mm thick CaF₂ crystal. The ring image forms directly in the UV-sensitive detector, with a dispersion that depends on the radiator thickness.
- Fig. 16 : Examples of single events obtained with the detector illustrated in the previous figure, for 1.3 GeV/c protons. The central point, corresponding to the charged particle trajectory is often accompanied by photon points emitted in the MSC window.
- Fig. 17 : Measured distribution in the number of photons obtained with the detector shown in Fig. 15, for 1.3 and 1.5 GeV/c protons (point with error bars). The histogram corresponds to a Poisson distribution with the indicated average.
- Fig. 18 : Measured distribution of the average ring radius (points with error bars). The full curves represent a Gaussian fit with the indicated average values and standard deviations.

- Fig. 19 : Computed Čerenkov angle in a LiF radiator with $n = 1.50$, as a function of particle momentum for pions and protons. The points with error bars correspond to the measured values at 1.3 and 1.5 GeV/c, obtained from the previous figure and the known geometry (Fig. 15).
- Fig. 20 : Extrapolation of our results to a 10 atm, 50 cm long argon radiator using the MSC Čerenkov imaging device. The strips show the expected radius and angle resolution (one standard deviation around the average) for an $f = 50$ cm optics, as well as the expected number of photons N and the corresponding inefficiency levels if three or more photons are required for an event to be reconstructed.
- Fig. 21 : Pulse-height spectra obtained in an MSC having a proportional chamber in the last element with a 5 mm thick LiF radiator under Čerenkov emission conditions (larger peak, protons at 1.5 GeV/c) and total reflection conditions (smaller peak, pions at 1.5 GeV/c). The residual signal, in the second case, that coincides with the spectrum obtained for both particles turning the detector by 180° in respect to the beam, is given both by direct ionization in the gas of the MSC and by scintillation in the radiator. Removing the sensitive part of the detector from the beam, one may obtain virtual insensitivity for particles having a velocity above the total reflection limit.

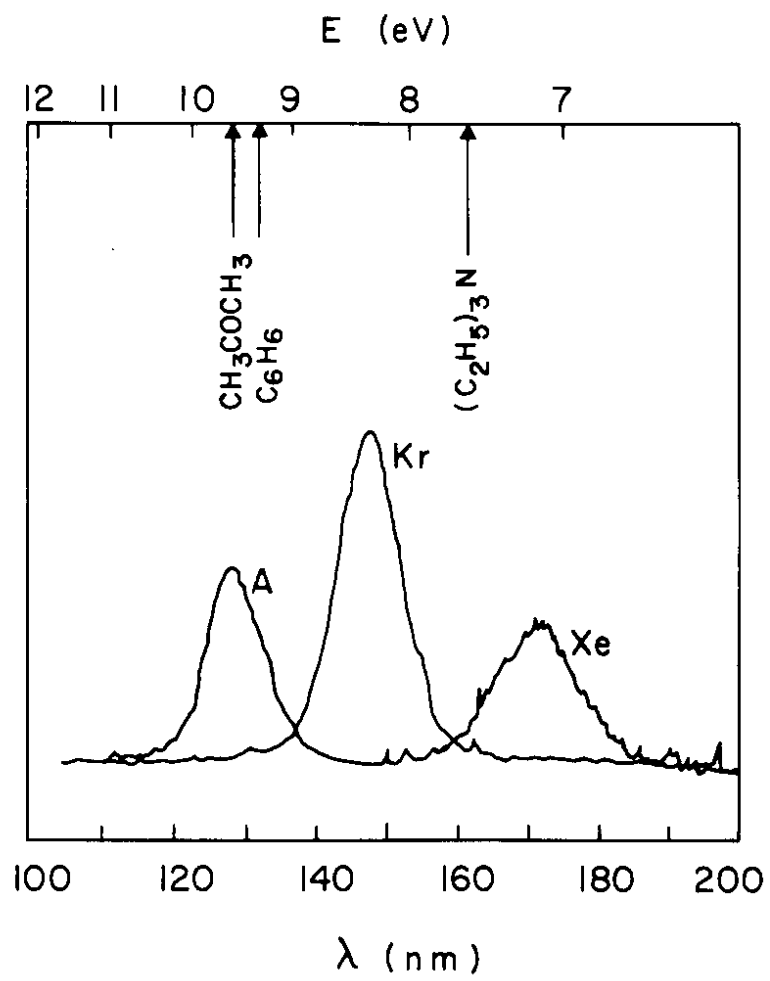


Fig. 1

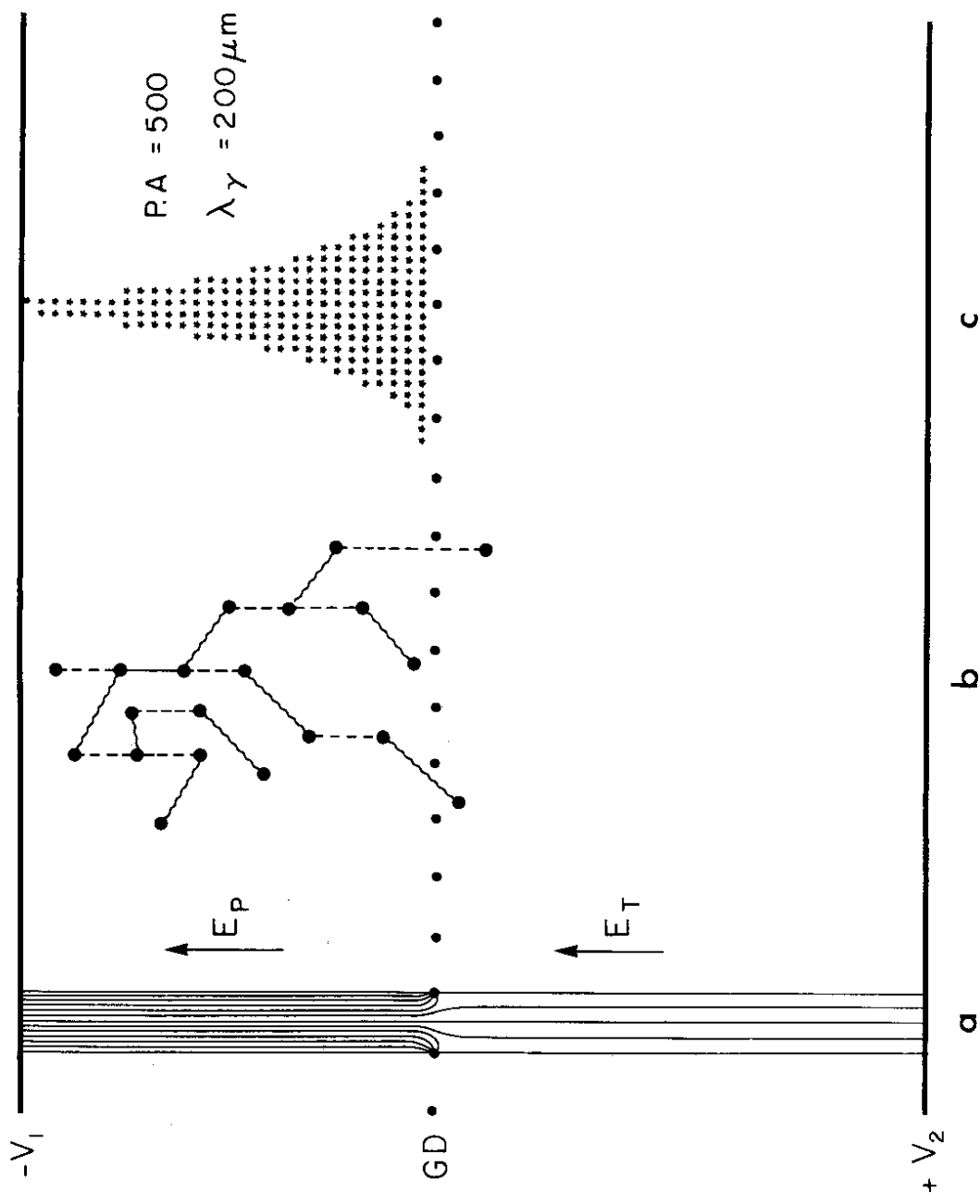


Fig. 2

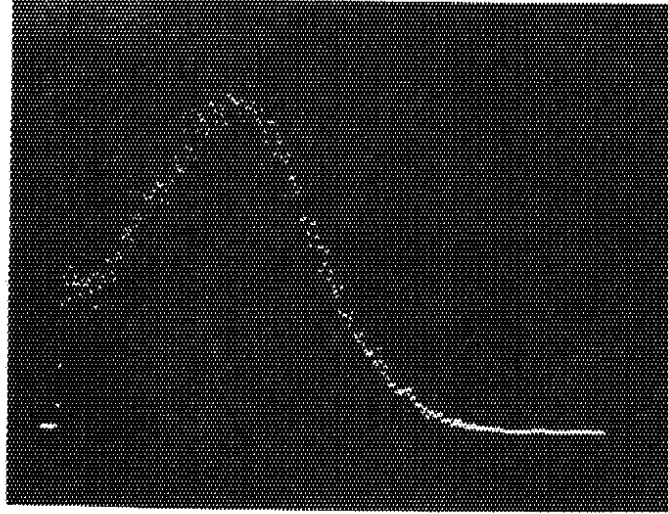


Fig. 3

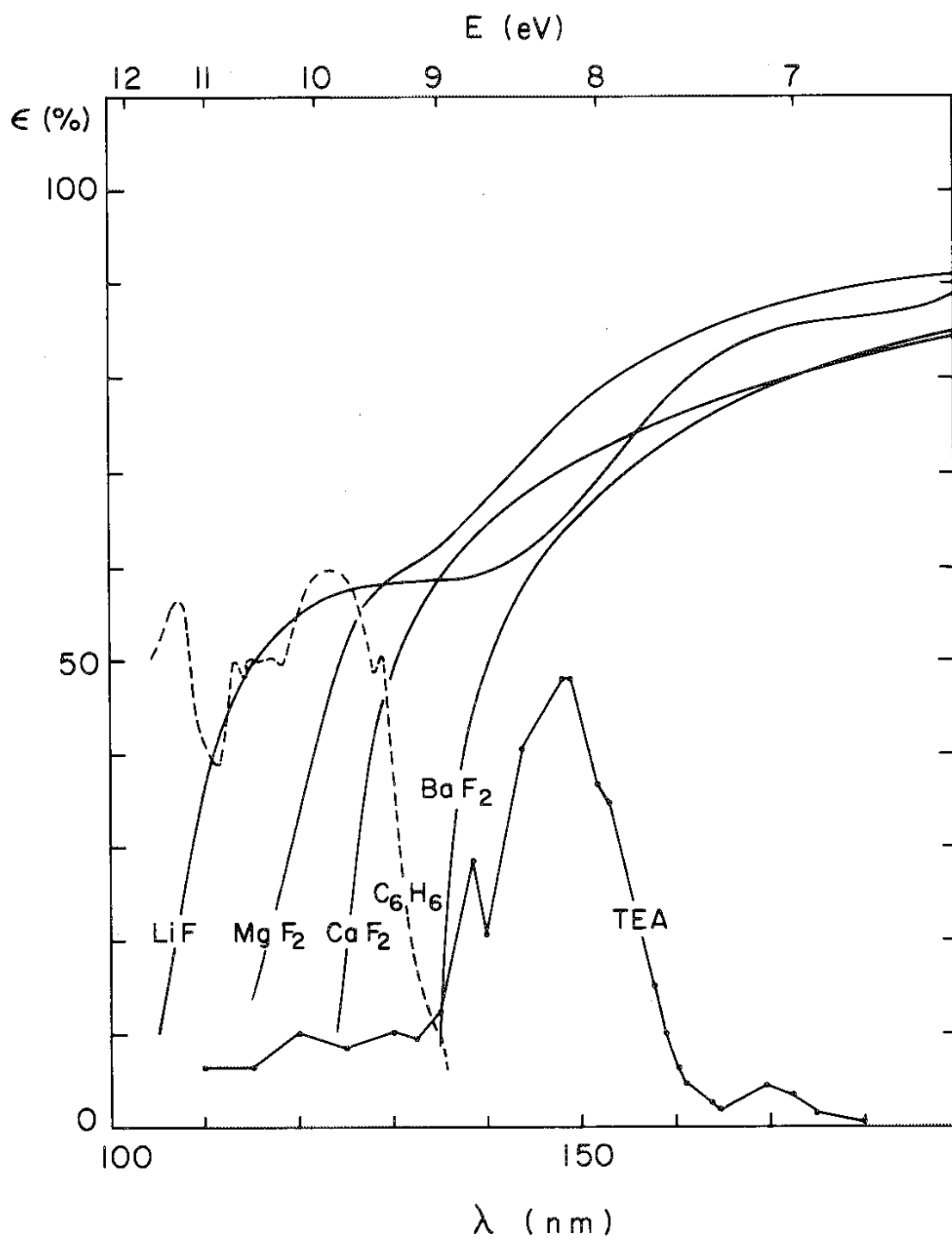


Fig. 4

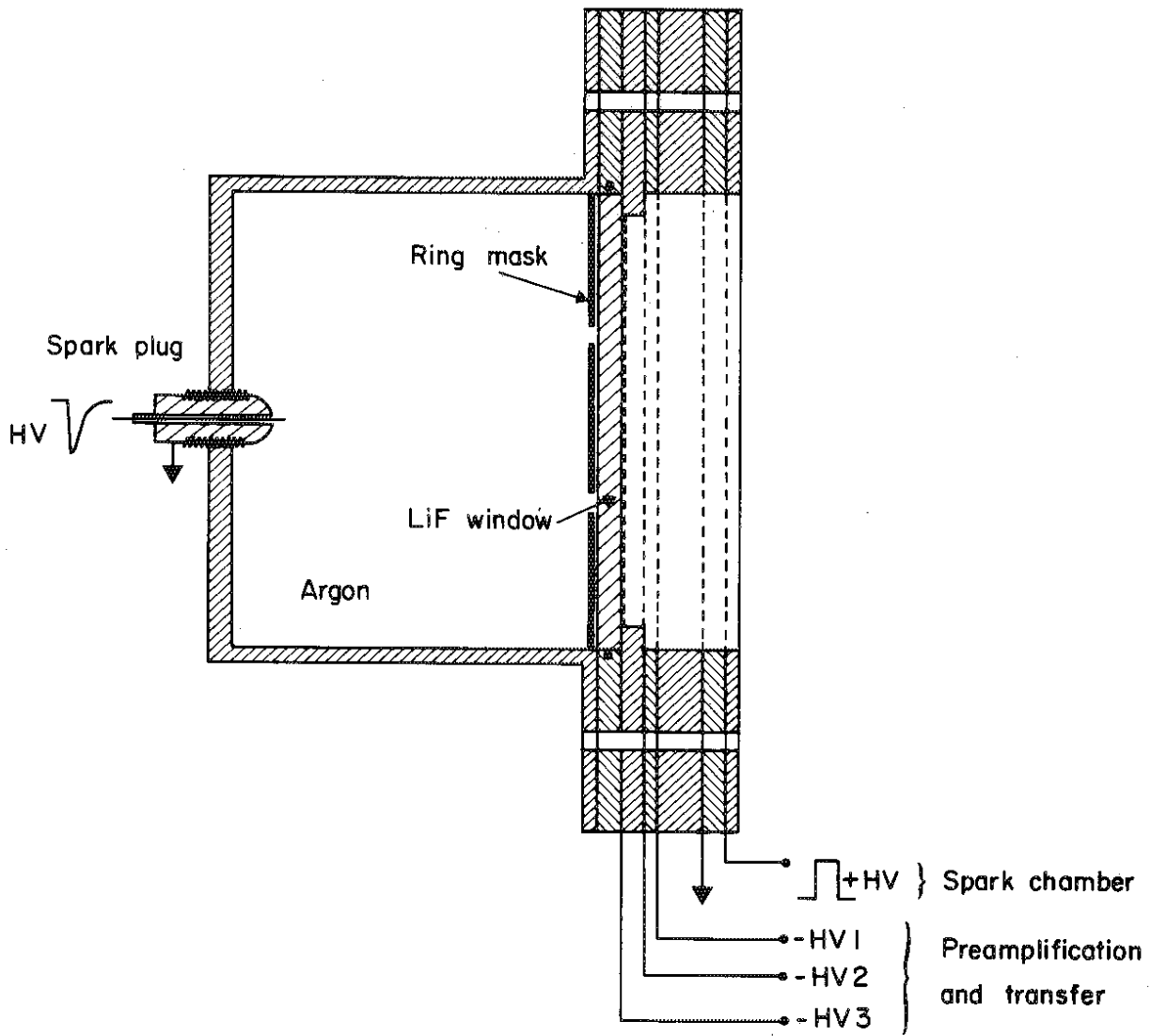
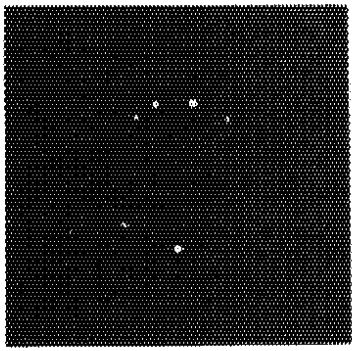
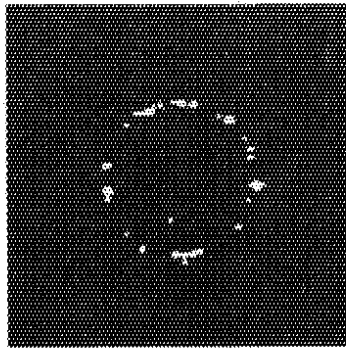


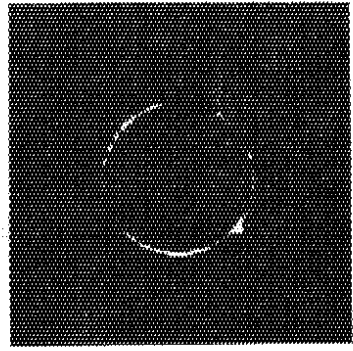
Fig. 5



a

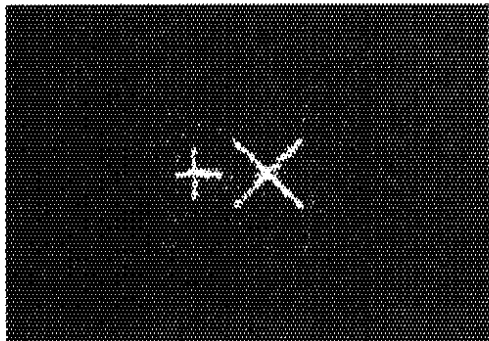


b

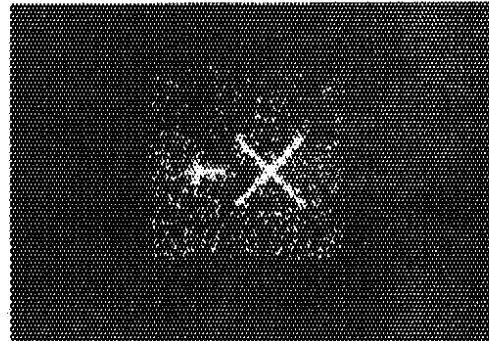


c

Fig. 6



a



b

Fig. 7

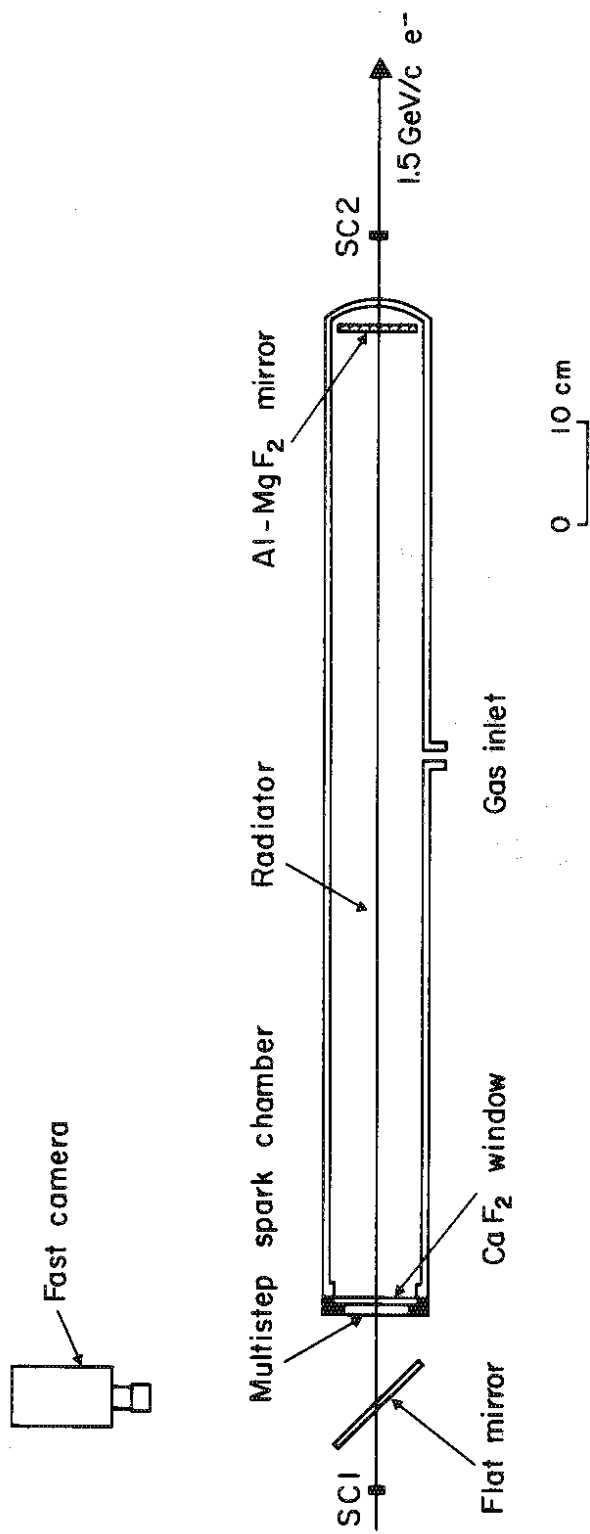


Fig. 8

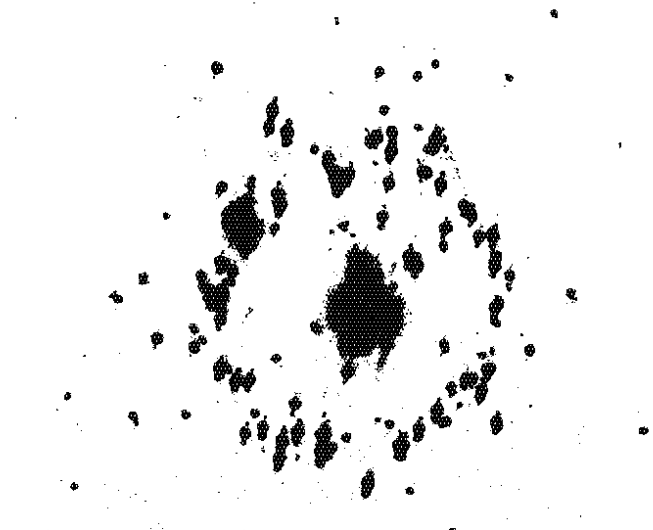


Fig. 9

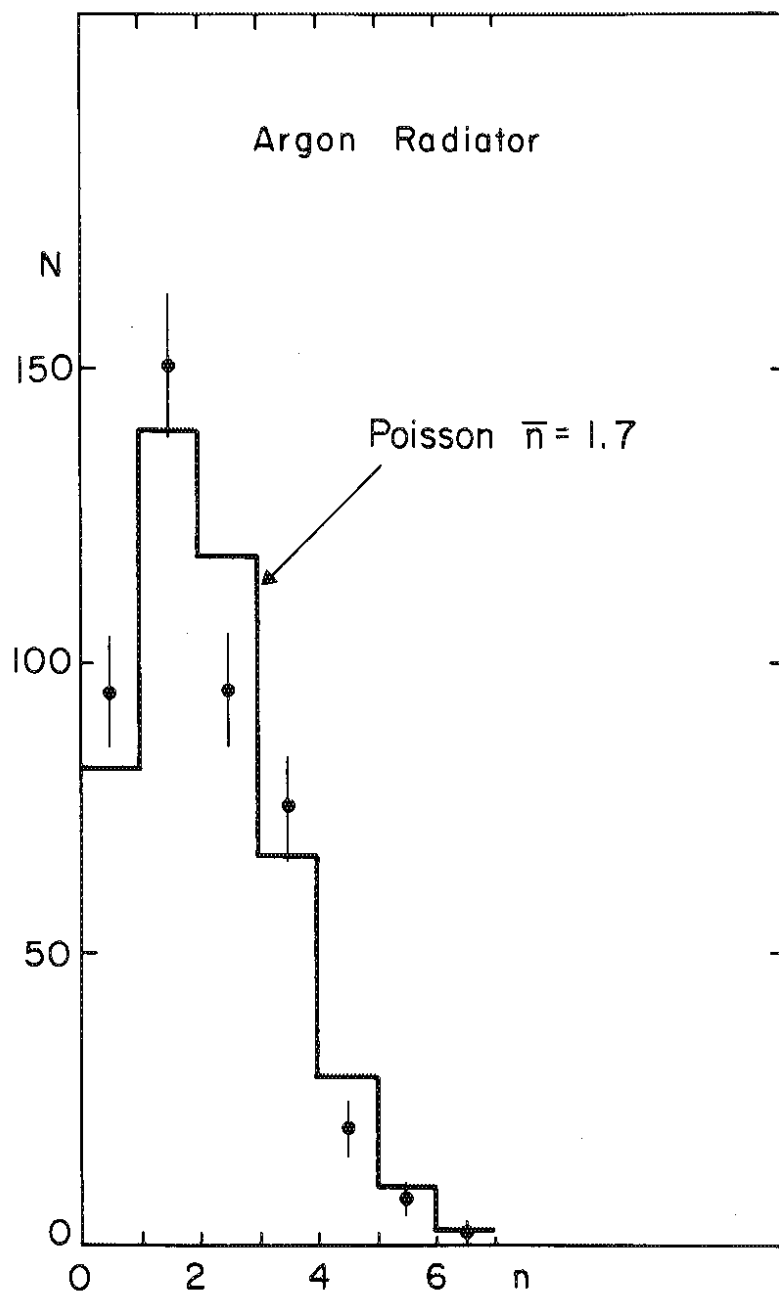


Fig. 10

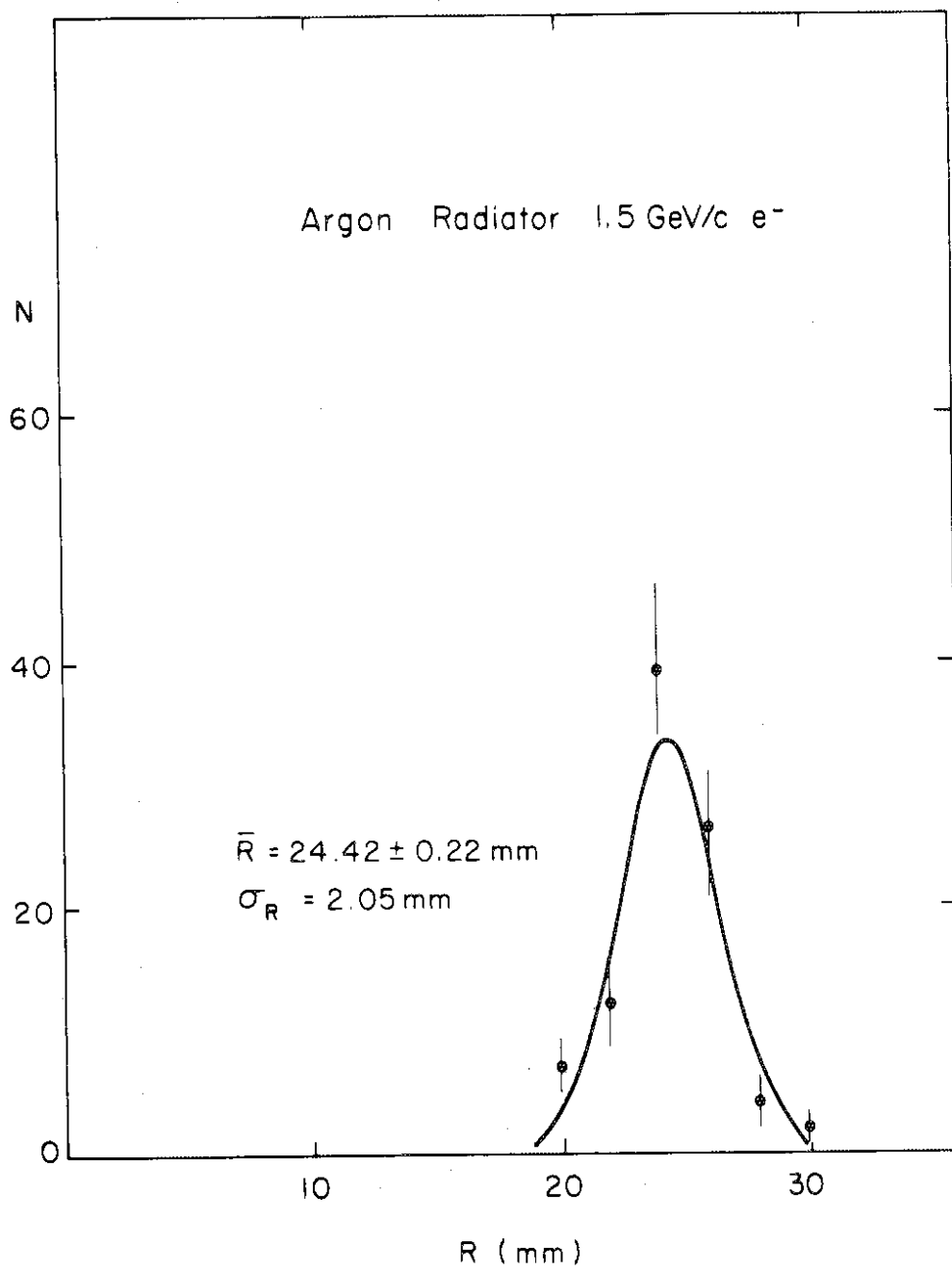


Fig. 11

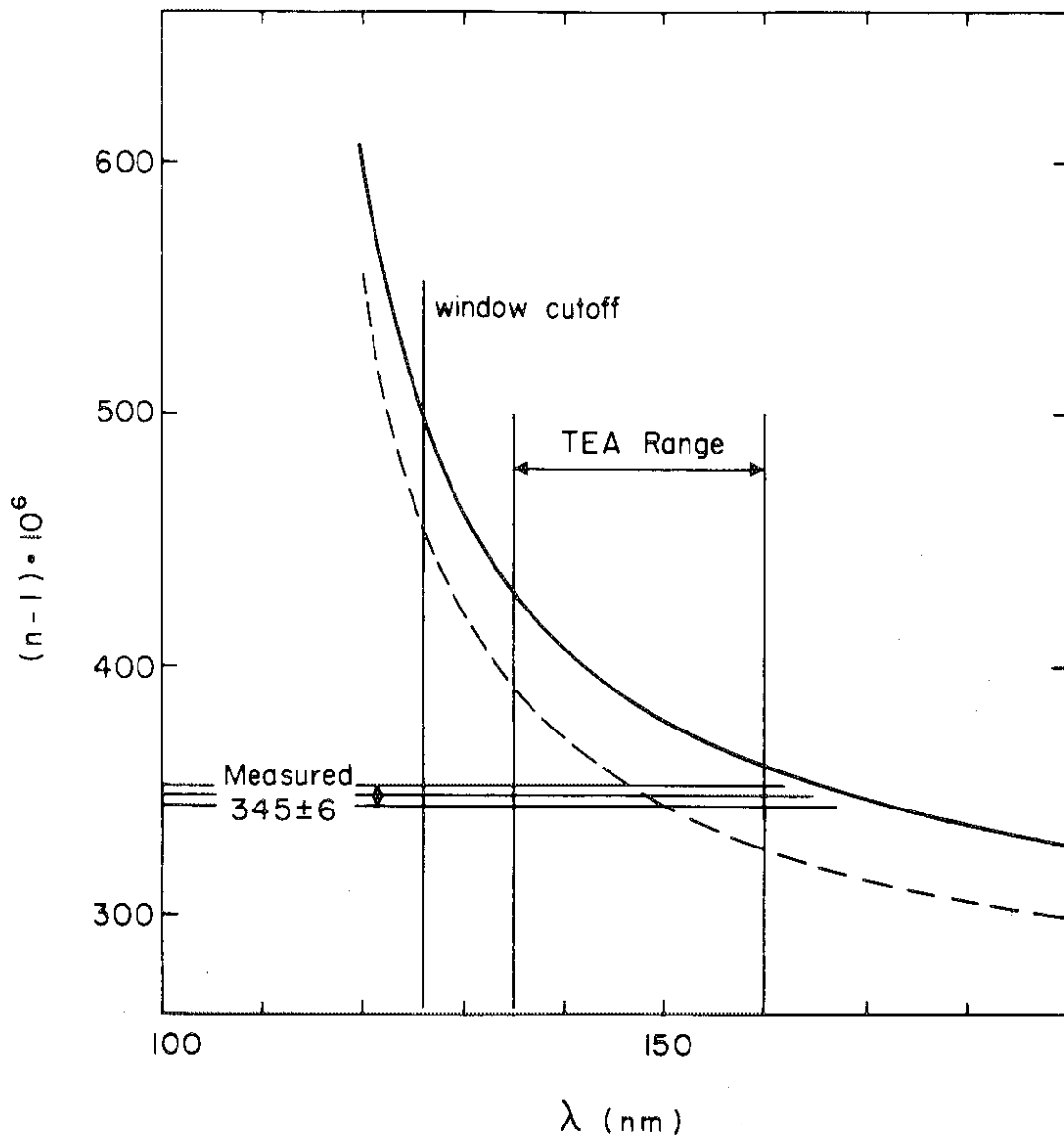


Fig. 12

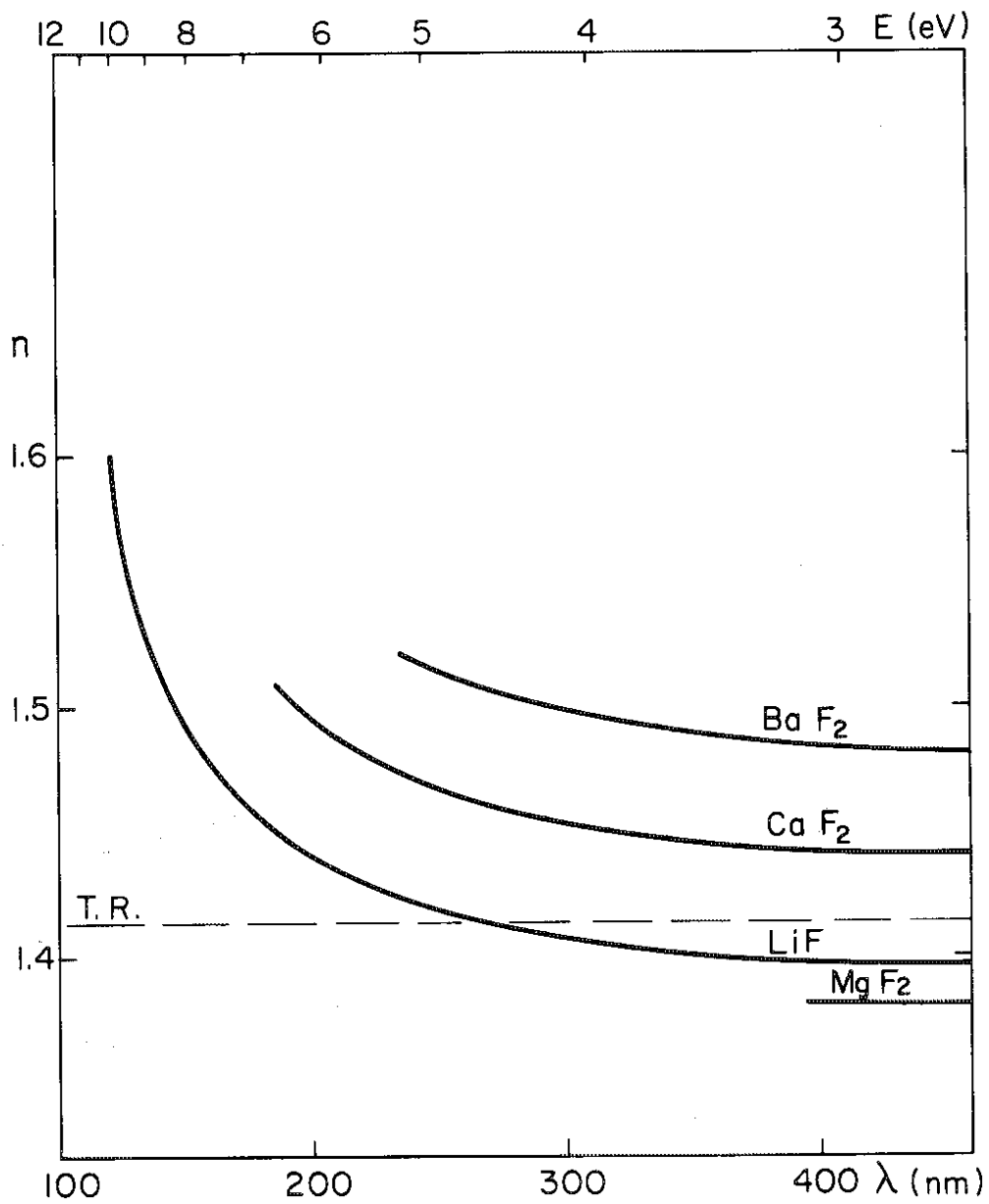
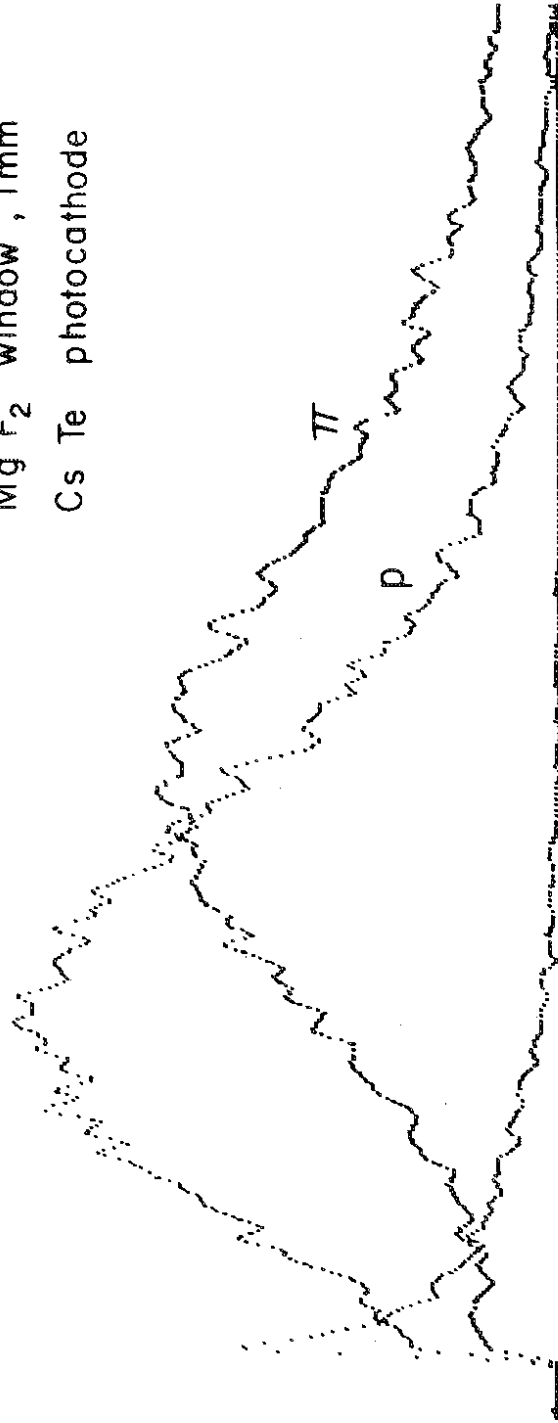


Fig. 13

1.5 GeV/c EMI 626H315

Mg F₂ window, 1mm
Cs Te photocathode



Pulse Height

Fig. 14

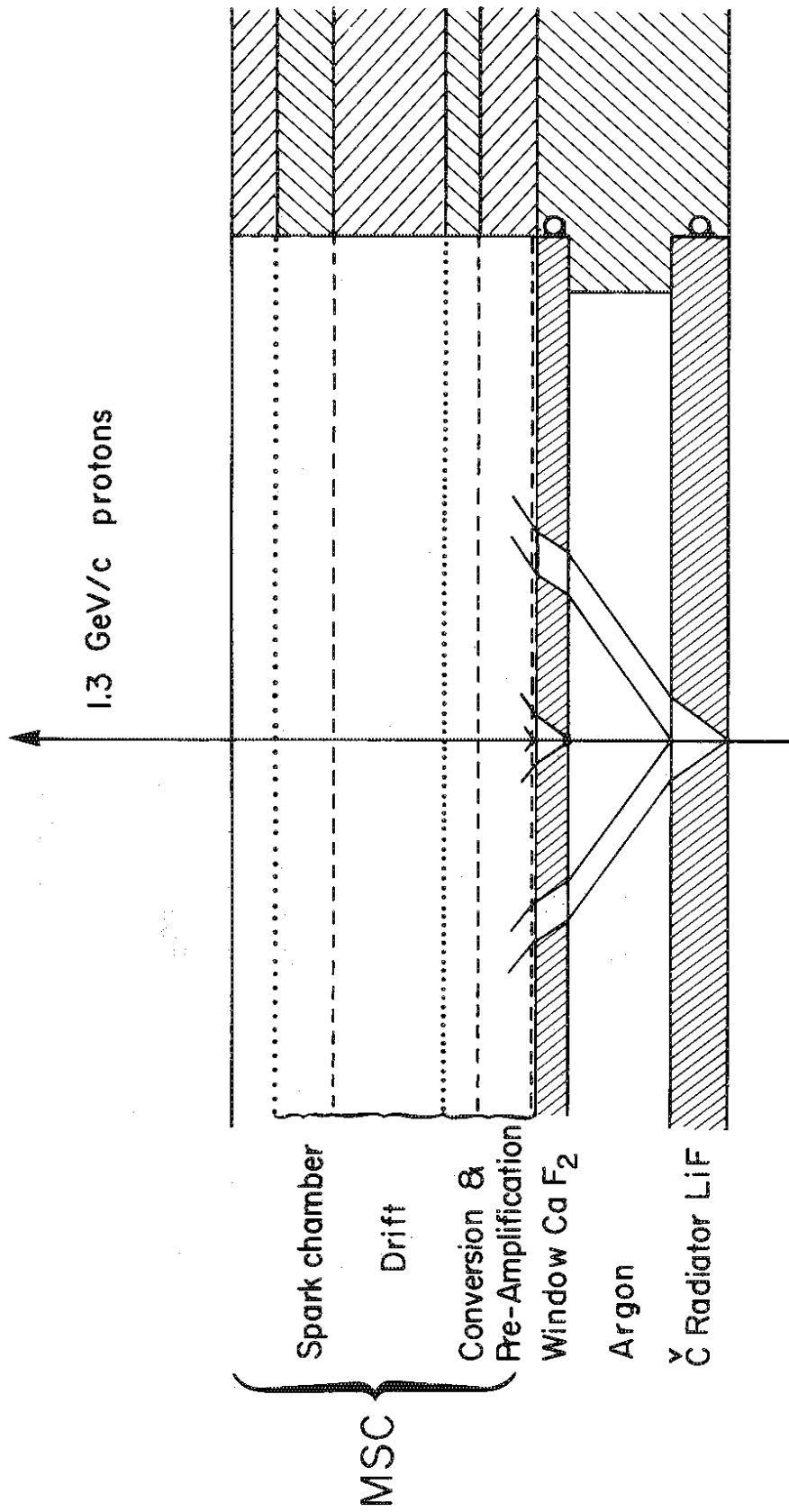


Fig. 15

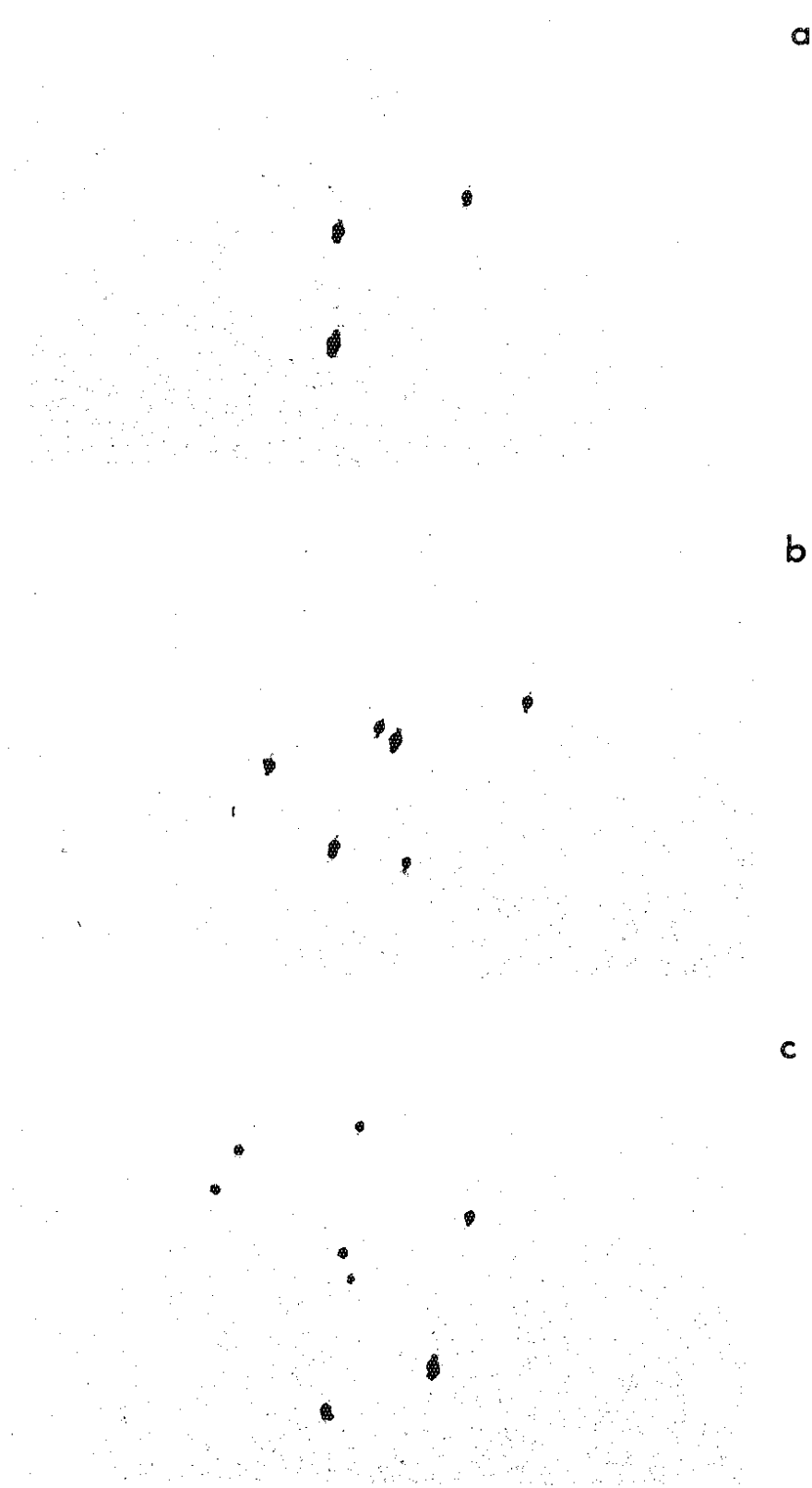


Fig. 16

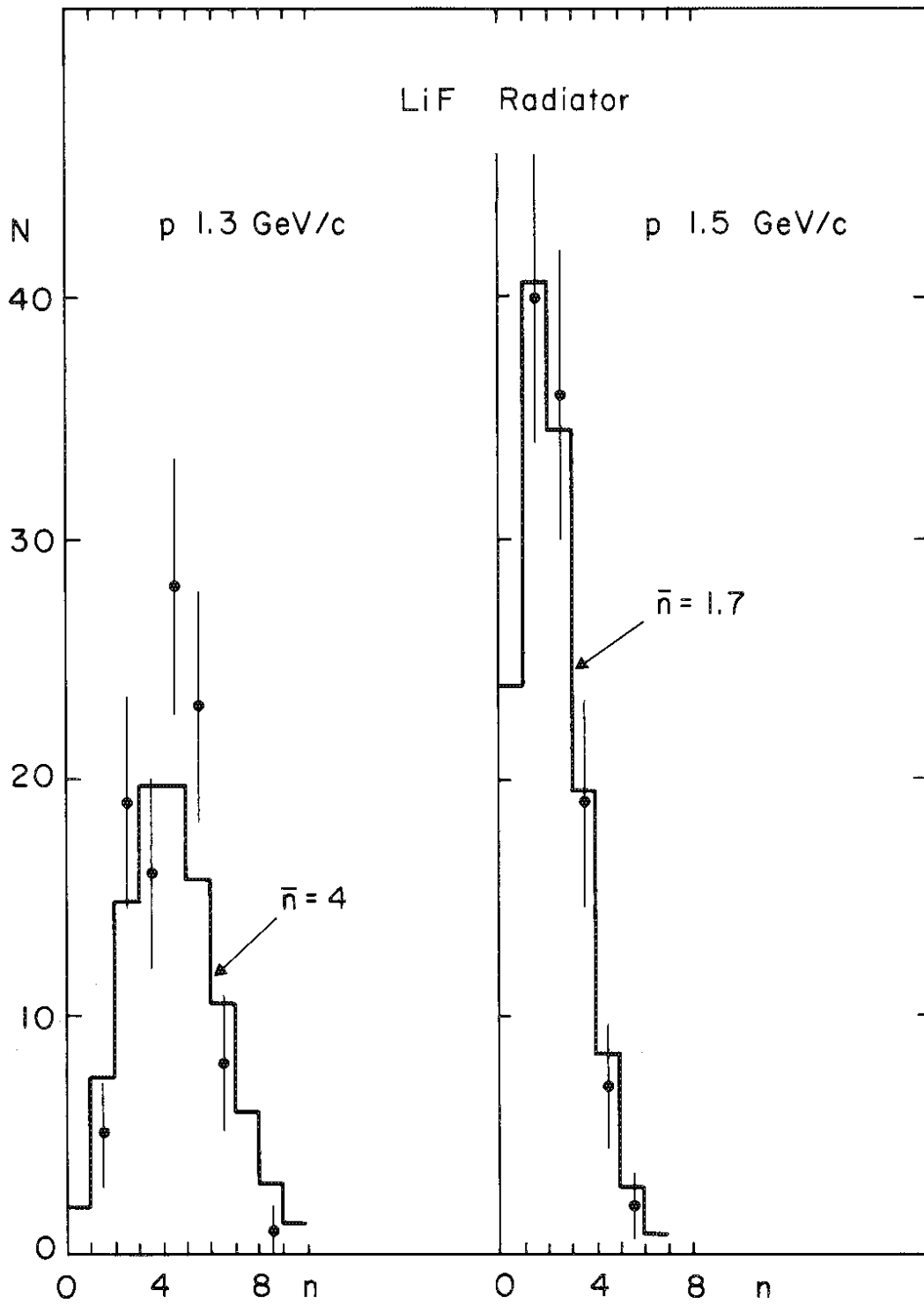


Fig. 17

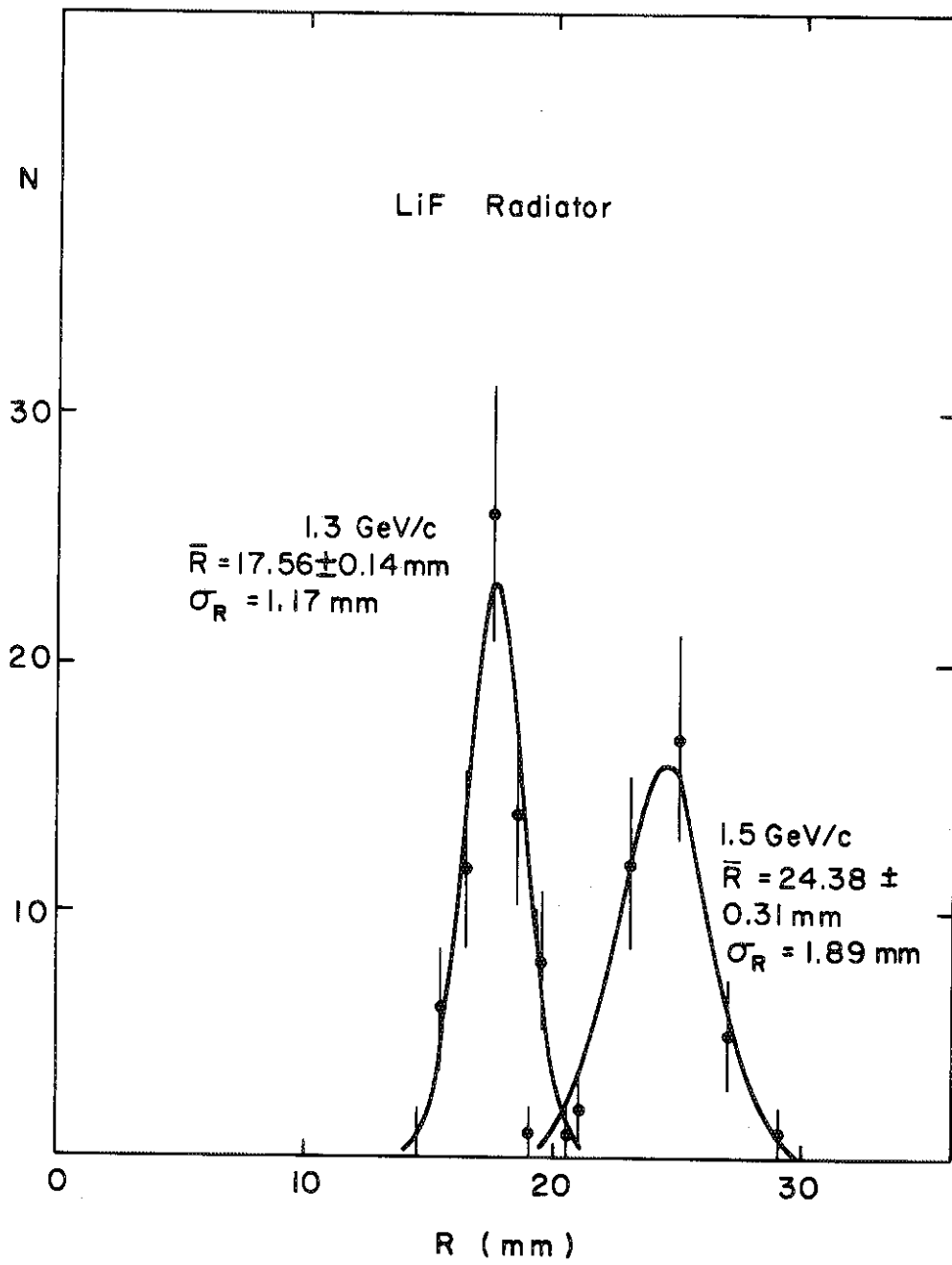


Fig. 18

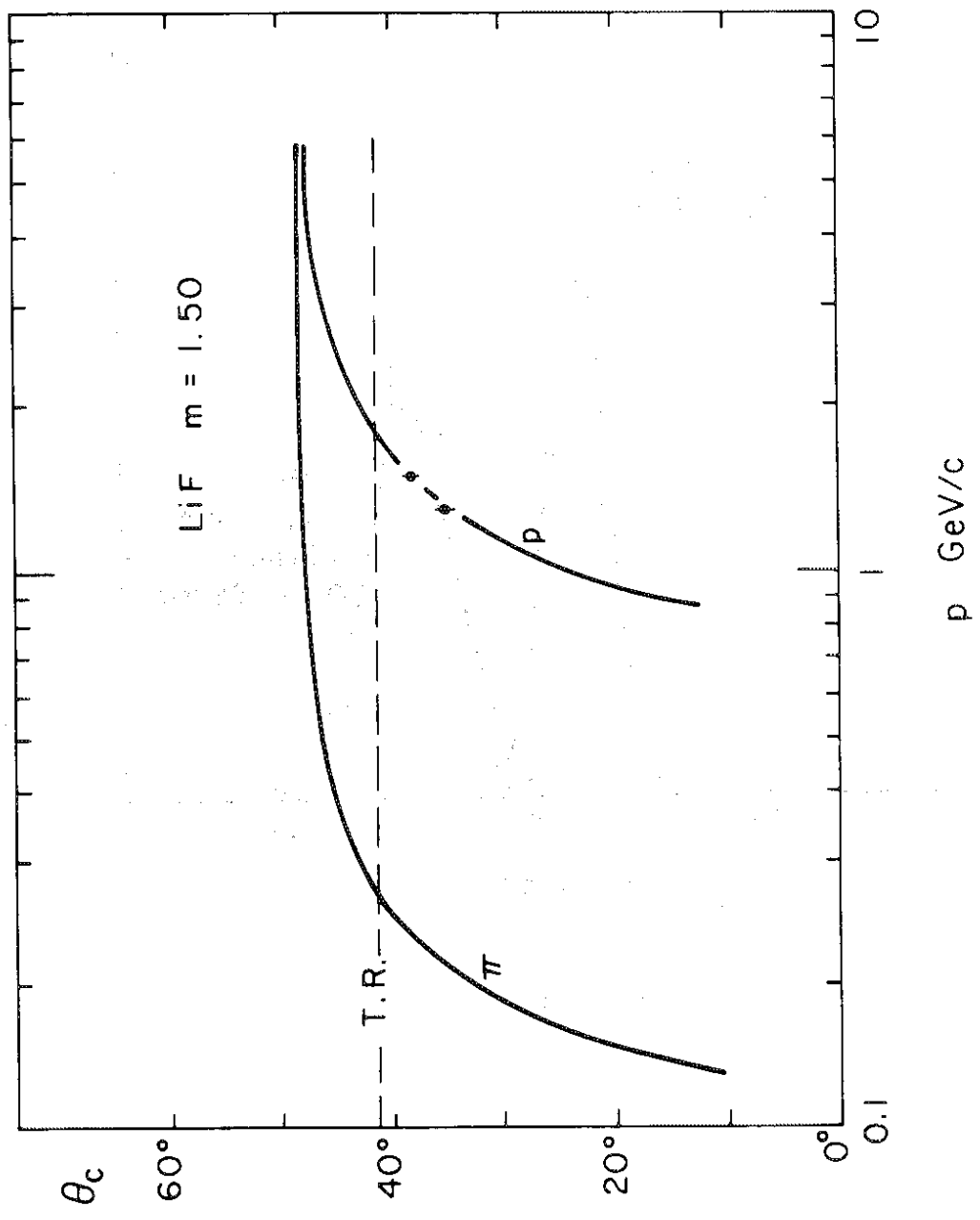


Fig. 19

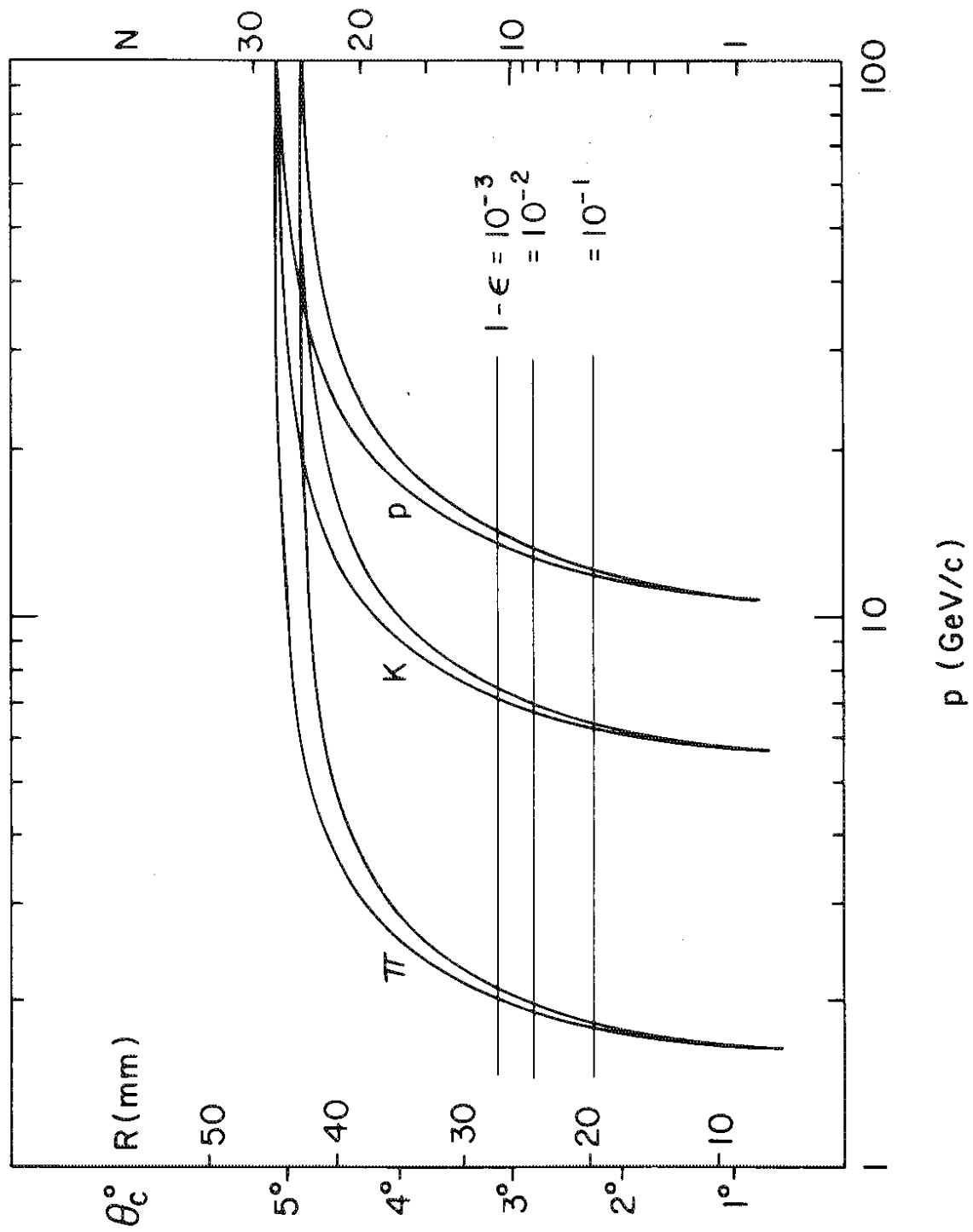


Fig. 20

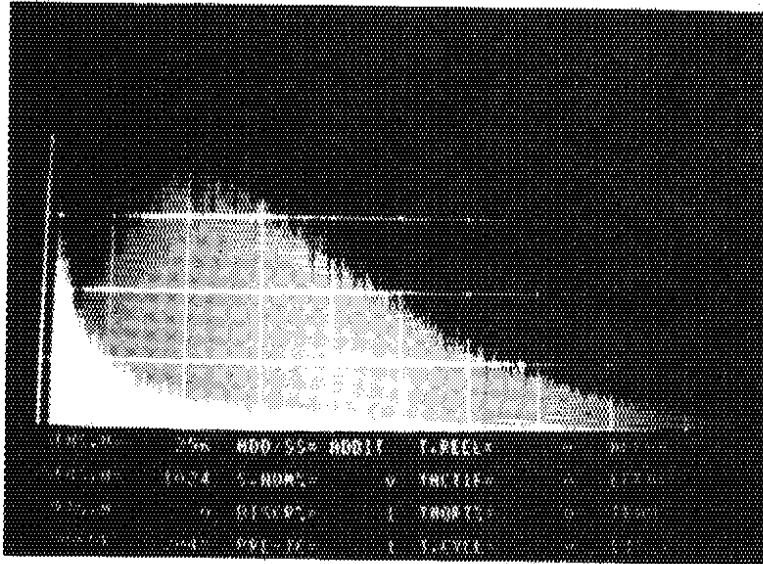


Fig. 21